Effectiveness of precursor emission reductions for the control of summertime ozone and $PM_{2.5}$ in the Beijing–Tianjin–Hebei region under different meteorological conditions

Jing QIAN, and Hong LIAO*

Jiangsu Key Laboratory of Atmospheric Environment Monitoring and Pollution Control, Jiangsu Engineering Technology Research Center of Environmental Cleaning Materials, Collaborative Innovation Center of Atmospheric Environment and Equipment Technology, School of Environmental Science and Engineering, Nanjing University of Information Science & Technology, Nanjing, Jiangsu, China

ABSTRACT

We used the observed concentrations of air pollutants, reanalyzed meteorological parameters, and the results from the Goddard Earth Observing System Chemical Transport Model (GEOS-Chem) to examine the relationships between maximum daily 8 h average ozone (MDA8 O_3), $PM_{2.5}$ (particulate matter with diameter of 2.5 μm or less), $PM_{2.5}$ components and 2 m temperature (T2)/relative humidity (RH) as well as the effectiveness of precursor emission reductions on the control of O_3 and $PM_{2.5}$ in Beijing–Tianjin–Hebei (BTH) under different summertime temperature and humidity conditions. Both observed (simulated) MDA8 O_3 and $PM_{2.5}$ concentrations increased as T2 went up, with linear trends of 4.8 (3.2) ppb $℃^{-1}$ and 1.9 (1.5) μg m^{-3} $℃^{-1}$, respectively. Model results showed that the decreases in MDA8 O_3 from precursor emission reductions were more sensitive to T2 than to RH. Reducing a larger proportion of volatile organic compounds (VOCs) emissions at higher T2 was more effective for the control of

*Corresponding author: Hong LIAO
Email: hongliao@nuist.edu.cn

summertime O_3 in BTH. For the control of summertime $PM_{2.5}$ in BTH, nitrogen oxides (NO_x) reduction combined with a small proportion reduction of VOCs was the best measure. The magnitude of reduction in $PM_{2.5}$ from reducing precursor emissions was more sensitive to RH than to T2, with the best efficiency at high RH. Results from this study are helpful for formulating effective policies to tackle O_3 and $PM_{2.5}$ pollution in BTH.

Key words: Ozone; $PM_{2.5}$; Emission reductions; Meteorological conditions

Article Highlights:

- Observed summertime concentrations of O_3 and $PM_{2.5}$ in BTH increased as T2 and RH increased (when RH < 60%).
- Larger percentage reduction of VOCs emissions at higher temperature is more effective for alleviating summertime O_3 pollution in BTH.
- NO_x reduction combined with a small proportion reduction of VOCs is the best measure for $PM_{2.5}$, which has the best effect at high RH.
- For the co-pollution of O_3 and $PM_{2.5}$ in summer in BTH, emission reductions have the best effect in a hot and humid conditions.

https://doi.org/10.1007/s00376-024-4071-4

1. Introduction

China has high concentrations of both $PM_{2.5}$ (particulate matter with an aerodynamic equivalent diameter of 2.5 μm or less) and tropospheric ozone (O_3), especially in the Beijing-Tianjin-Hebei (BTH) region, a major urban cluster with developed economies in eastern China (Luo et al., 2022; Dai et al., 2023). Over 2013–2019, the summer (June–July–August, JJA) mean maximum daily 8 h average (MDA8) O_3 concentrations were observed to increase at a rate of 3.3 ppb y^{-1} over the North China Plain (NCP) (Li et al., 2020). In spite of the effective control of $PM_{2.5}$ pollution in China since the implementation of Clean Air Action in 2013, the annual mean $PM_{2.5}$ concentration averaged over the BTH was 44 μg m^{-3} in 2022 (https://www.mee.gov.cn/hjzl/sthjzk/zghjzkgb/), which still far exceeded the air quality standard of 5 μg m^{-3} set by the World Health Organization. Further efforts are needed to control O_3 and $PM_{2.5}$ pollution in BTH (Zhao et al., 2021).

Variations of O_3 and $PM_{2.5}$ are highly sensitive to changes in meteorology. While wind, precipitation, and planetary boundary layer height may influence the dispersion, wet removal, and vertical mixing of air pollutants (Chen et al., 2020; Zhang and Wang, 2020), temperature and relative humidity (RH) play important roles in the formation of secondary pollutants and the gas-particle partitioning of semi-volatile components (Wang et al., 2013; Shah et al., 2018; Leung et al., 2020). Higher temperature can accelerate the chemical production of O_3, while higher RH increases the O_3 loss (Johnson et al., 1999; Jacob and Winner, 2009). As for $PM_{2.5}$, higher temperature can enhance gas phase reaction rates and oxidant concentrations, leading to higher sulfate (SO_4^{2-}) concentrations (Liao et al., 2006). However, higher temperature can promote the volatilization of ammonium nitrate (Kleeman, 2008). Higher RH is conducive to aqueous phase aerosol

chemistry for the formation of secondary $PM_{2.5}$ (Dawson et al., 2007; Zheng et al., 2015). Li et al. (2019a) showed by a stepwise multiple linear regression (MLR) model that the changes in daily maximum 2 m temperature (Tmax), 10 m meridional wind, and RH explained 66% of monthly variability in summer MDA8 O_3 in BTH over 2013−2017. By applying the Goddard Earth Observing System Chemical Transport Model (GEOS-Chem) and the Lindeman, Merenda, and Gold (LMG) method, Dang et al. (2021) found that the changes in Tmax and RH explained, respectively, 31% and 11% of the simulated interannual variations of MDA8 O_3 in JJA of 2012–2017 over NCP in the simulation with changes in meteorological parameters alone. Zong et al. (2021) analyzed the synoptic weather pattern corresponding to the cooccurrence of O_3 and $PM_{2.5}$ pollution during summer of 2015–2018 over eastern China by applying the T-mode principal component analysis, and found that the warm and moist flow brought by the western Pacific subtropical high promoted hygroscopic growth of the fine particulate matter, resulting in the increases in $PM_{2.5}$ concentrations in BTH.

Emission reduction is the primary measure for controlling air pollution. Owing to the absence of effective emission control measures on volatile organic compounds (VOCs) in previous policies in China, anthropogenic VOCs emissions in China were estimated to increase from 25.9 Tg in 2010 to 28.6 Tg in 2017 (increase by 11%) according to the Multi-resolution Emission Inventory for China (Zheng et al., 2018). In the 14th Five-Year Plan for 2021–2025, China identifies VOCs emission management as a prioritization in order to further improve air pollution. In addition, as a common and important precursor of O_3 and $PM_{2.5}$, the continuous control of nitrogen oxides (NO_x = $NO + NO_2$) emissions remains a key focus of air pollution control. A number of studies

have examined VOCs and NO_x emission reduction strategies for the synergistic reduction of ambient O_3 and $PM_{2.5}$ pollution. By using simulations from the GEOS-Chem for summer of 2017, Li et al (2019b) evaluated the effects of the reduction targets for 2018–2020 (i.e., 9% for NO_x emissions, 10% for VOCs emissions and 8% for $PM_{2.5}$ concentrations) over NCP, and showed that the increases in O_3 owing to the decreases in $PM_{2.5}$ were offset by the decreases in O_3 owing to the decreases in NO_x and VOC emissions, resulting in the reduction of about 1 ppb in seasonal mean MDA8 O_3. Xiang et al. (2020), by applying Weather Research and Forecasting model (WRF) with Chemistry together with an empirical kinetics modeling approach to conduct multiple scenario analyses for reduction of anthropogenic NO_x and VOCs emissions over the BTH and surrounding areas relative to January and July of 2015–2017, and suggested that, from a long-term perspective, reducing firstly VOCs emissions by about 60% and NO_x emissions by about 20% to avoid the rebound of O_3 and then phasing out the remaining emissions to reach a deep mitigation. Ding et al. (2022) adopted the Community Multiscale Air Quality (CMAQ) model, WRF model, and the extended response surface model with polynomial functions, and reported that no matter how much VOCs emissions was reduced, NO_x emission reduction (64%−81%) was essential to attain the air quality standard (with the annual $PM_{2.5}$ concentration ≤ 35 μg m^{-3} and the annual 90th percentile MDA8 O_3 concentration ≤ 160 μg m^{-3}) in BTH in 2017, in which year the observed annual concentrations of O_3 and $PM_{2.5}$ were 178−216 μg m^{-3} and 57−86 μg m^{-3}, respectively. These studies with the impacts of VOCs and NO_x emission reductions on O_3 and $PM_{2.5}$ were generally based on the average over time scales (i.e., monthly, seasonal, annual), ignoring the impacts of variations in meteorological fields on control

measures. Therefore, it is essential to examine the effectiveness of precursor emission reductions for the control of O_3 and $PM_{2.5}$ pollution under different conditions of temperature and humidity so as to formulate more effective policies.

The objectives of this study are (1) to examine the relationships between concentrations of O_3 and $PM_{2.5}$ and T2/RH based on the observations from Chinese Ministry of Ecology and Environment (MEE) and the reanalyzed meteorological parameters from Version 2 of Modern-Era Retrospective analysis for Research and Application (MERRA-2) over BTH for summer of 2019, (2) to apply the GEOS-Chem model that can capture the observed relationships to quantify the effectiveness of emission reductions of VOCs and NO_x on O_3 and $PM_{2.5}$ in BTH under different conditions of temperature and humidity, and (3) to identify the temperature and humidity conditions under which emission reductions have the best effect for alleviating summertime O_3 and $PM_{2.5}$ pollution in BTH. Year 2019 was selected because MDA8 O_3 concentrations in this year were among the highest in recent years, and the concentrations of $PM_{2.5}$ in 2019 were still at a relatively high level in BTH.

The remainder of this paper is structured as follows. Section 2 describes the observations, reanalyzed meteorological data, GEOS-Chem model, and numerical experiments. The model evaluation, the relationships between atmospheric oxidants, O_3, $PM_{2.5}$, and $PM_{2.5}$ components and T2/RH, as well as the simulated changes of all these species under different temperature and humidity conditions with emission reductions of VOCs and/or NO_x are presented in Section 3. Section 4 summarizes the main conclusions.

2. Methods

2.1 Observed O_3 and $PM_{2.5}$ concentrations

The observed hourly concentrations of O_3 and $PM_{2.5}$ for JJA of year 2019 were obtained from MEE and can be downloaded from https://quotsoft.net/air/ (Wang, 2024). There are over 1600 observational sites throughout the country, in which 79 are located in Beijing–Tianjin–Hebei (BTH) region (37–41°N, 114–118°E). Concentrations were reported by the MEE in micrograms per cubic meter (μg m^{-3}) under reference state (298 K, 1013 hPa) for O_3 and under local ambient state for $PM_{2.5}$. For the consistency between observed and simulated O_3 concentrations, we converted the unit of observed O_3 to parts per billion (ppb). For O_3, MDA8 was used in this study, which was calculated when there were valid hourly data for at least 6 h for each 8 h and there were more than 14 valid 8 h averaged data in each day. Daily mean $PM_{2.5}$ concentration was calculated when there were valid hourly data for more than 20 h during that day. All the site concentrations were averaged within each of the 0.5° latitude × 0.625° longitude grid cells of MERRA-2 for model evaluation and subsequent analysis, following Dai et al. (2023). There are 18 model grids in BTH. We consider each day of each grid cell as an independent sample.

2.2 Reanalyzed meteorological data

Meteorological fields for 2019 were obtained from MERRA-2 generated by the NASA Global Modeling and Assimilation Office (GMAO). The MERRA-2 data have a horizontal resolution of 0.5° latitude × 0.625° longitude. Meteorological parameters considered in the study include 2 m temperature (T2), RH, and precipitation (PR). The temporal resolution for T2 and PR is 1 h, and that for RH is 3 h. Note that T2 and RH are averaged over 24 h, while PR is summed over 24 h. We do not consider days with precipitation, samples with total daily precipitation greater than 0.1 mm were removed.

Meanwhile, after removing the days with missing data of MDA8 O_3 or $PM_{2.5}$, there are ultimately 620 valid samples remaining out of 1656 samples over BTH in JJA of 2019. To explore the effects of precursor emission reductions on MDA8 O_3 and $PM_{2.5}$ under different conditions of temperature and humidity, T2 are binned to 2°C intervals and RH are binned to 5% intervals.

2.3 GEOS-Chem model

The simulations of air pollutants for JJA of year 2019 were carried out by using the nested version of GEOS-Chem (version 11-01, http://wiki.seas.harvard.edu/geos-chem/index.php/GEOS-Chem_v11-01), driven by the MERRA-2 assimilated meteorological fields (Gelaro et al., 2017). The nested version of v11-01 in the Asian (11°S–55°N, 60°E–150°E) has a horizontal resolution of 0.5° latitude × 0.625° longitude and 47 vertical layers up to 0.01 hPa, with dynamical boundary conditions from a global GEOS-Chem simulation by 2° latitude × 2.5° longitude horizontal resolution. The O_3 and $PM_{2.5}$ simulation in the GEOS-Chem model has been extensively used in previous studies (Fu and Liao, 2014; Zhang et al., 2018; Wang and Liao, 2020; Gong et al., 2022). The GEOS-Chem model includes a fully coupled O_3-NO_x-hydrocarbon chemistry (Bey et al., 2001; Park et al., 2004) and aerosols including sulfate (Park et al., 2004), nitrate (NO_3^-) (Pye et al., 2009), ammonium (NH_4^+), black carbon (BC) and organic carbon (OC) (Park et al., 2003), mineral dust (Fairlie et al., 2007), and sea salt (Alexander et al., 2005). Two primary organic aerosol (POA) tracers are considered in the model: hydrophobic and hydrophilic POAs. The hydrophobic POA becomes hydrophilic with an e-folding time of 1.15 days (Cooke et al., 1999; Park et al., 2003). It is assumed that 50% of POAs emitted are hydrophobic (Park

et al., 2003). The simulation of secondary organic aerosol (SOA) is based on the volatility basis set (VBS) approach. Reactions of forming SOA from different parent hydrocarbons can be mapped onto the same set of bins encompassing the range of typical ambient organic aerosol mass concentrations (~0.1–100 μg m^{-3}) (Jo et al., 2013). Wet deposition, including washout, rainout, and scavenging in moist convective updrafts, follows the scheme of Liu et al. (2001). Dry deposition is calculated based on the resistance-in-series model described by Wesely (1989) with a number of modifications (Wang et al., 1998).

The anthropogenic emissions of NO_x, carbon monoxide, OC, BC, sulfur dioxide (SO_2), and ammonia (NH_3) were obtained from MEIC (http://meicmodel.org.cn/) for year 2019, which includes emissions from the industry, power, residential, and transportation sectors. Due to the selection of a chemical mechanism developed by the State Air Pollution Research Center (SAPRC), namely SAPRC99, the downloaded MEIC data lack aromatics species that have a significant impact on SOA formation, such as benzene and toluene (Zhang et al., 2021; Wang et al., 2022). As a result, the anthropogenic emissions of VOCs (including ethane, propane, butanes, pentanes, other alkanals, ethene, propene, acetylene, benzene, toluene, xylene, formaldehyde, total ketones, and total acids) were obtained from Shared Socioeconomic Pathway (SSP) emission inventory (https://esgf-node.llnl.gov/projects/input4mips/). Year 2020 emissions of SSP2-4.5 were used in our simulations, which represent a middle-of-the-road development in the mitigation and adaptation challenges space. The biogenic emissions in GEOS-Chem were taken from MEGAN v2.1 (Guenther et al., 2012).

2.4 Numerical experiments

To investigate the effects of VOCs emission reductions on O_3 and $PM_{2.5}$ in BTH under different meteorological conditions, four numerical experiments were performed for JJA of 2019. Considering the recent national policies and the feasibility of practical control measures, the reduction ratios of anthropogenic VOCs were set between 10% and 50% with a 20% interval:

(1) CTRL: The control simulation without emission control measures;

(2) VOCs_10: The same as the CTRL simulation but with a 10% reduction in anthropogenic VOCs emissions in China;

(3) VOCs_30: The same as the CTRL simulation but with a 30% reduction in anthropogenic VOCs emissions in China;

(4) VOCs_50: The same as the CTRL simulation but with a 50% reduction in anthropogenic VOCs emissions in China;

Since NO_x also plays an important role in the formation of O_3 and $PM_{2.5}$, and the new 14th Five-Year Plan for 2021–2025 calling for a 10% decrease in NO_x emissions (https://www.mee.gov.cn/zcwj/zyygwj/202111/t20211108_959456.shtml), we also conducted three additional experiments:

(5) NO_x_10+VOCs_10: The same as the CTRL simulation but with a 10% reduction in both anthropogenic NO_x and anthropogenic VOCs emissions in China;

(6) NO_x_10+VOCs_30: The same as the CTRL simulation but with 10% and 30% reductions in anthropogenic NO_x and VOCs emissions in China, respectively;

(7) NO_x_10+VOCs_50: The same as the CTRL simulation but with 10% and 50% reductions in anthropogenic NO_x and VOCs emissions in China, respectively;

All the simulations were integrated for the period of 1 June to 31 August of year 2019 after a six month spin up of the model.

3. Results

3.1 Evaluation of model performance

Figures 1a and 1b present, respectively, the spatial distributions of simulated and observed surface-layer concentrations of MDA8 O_3 and $PM_{2.5}$ averaged over summer of 2019. For model evaluation, observed MDA8 O_3 and $PM_{2.5}$ concentrations were averaged over all sites within each of the 0.5° × 0.625° MERRA-2 grid cells. The concentrations of MDA8 O_3 and $PM_{2.5}$ were both relatively high in BTH. The seasonal mean observed (simulated) concentrations of MDA8 O_3 and $PM_{2.5}$ were 83.6 (71.9) ppb and 31.6 (32.1) μg m^{-3}, respectively, as values were averaged over the 18 grids in BTH. Figures 1c and 1d show the scatterplot of simulated versus observed daily MDA8 O_3 and $PM_{2.5}$ concentrations, respectively, for 18 grids located in BTH. The simulated spatiotemporal variations of MDA8 O_3 and $PM_{2.5}$ agree fairly well with the observations, with correlation coefficients (R) of 0.68 and 0.60, respectively. The model underestimates MDA8 O_3 concentrations with a normalized mean bias (NMB) of −11.7% and overestimates $PM_{2.5}$ concentrations with a NMB of +6.0% in BTH.

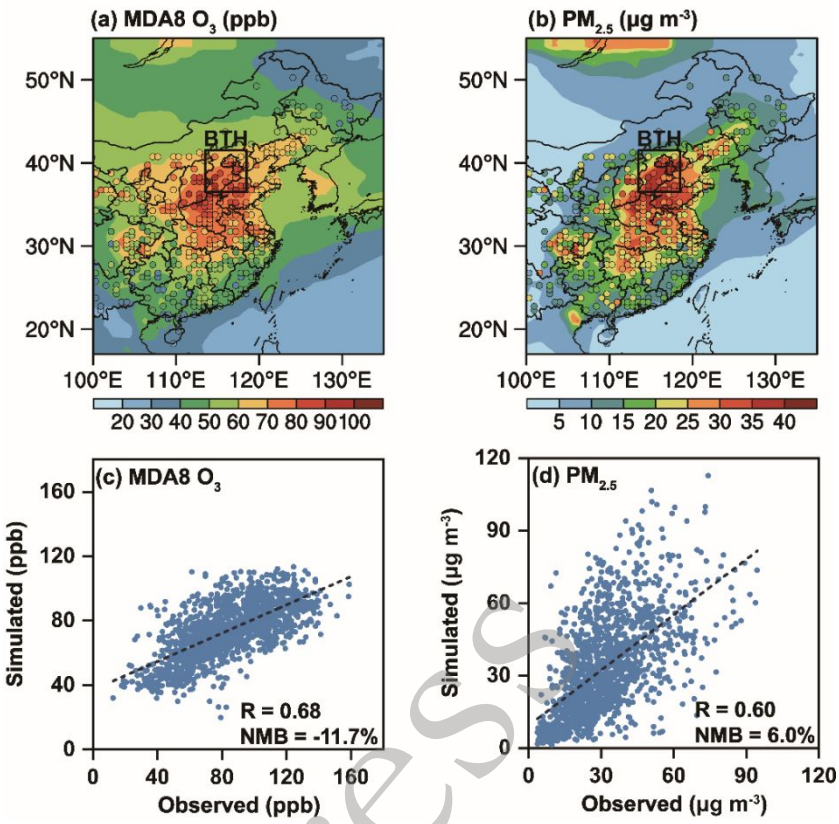

Fig. 1. Spatial distributions of simulated (shades) and observed (dots) surface-layer concentrations of (a) MDA8 O_3 (units: ppb) and (b) $PM_{2.5}$ (units: μg m^{-3}) averaged over summer in 2019. The solid black rectangles in (a−b) indicate the BTH region, which contain 18 grids. Scatterplot of simulated versus observed daily concentrations of (c) MDA8 O_3 (units: ppb) and (d) $PM_{2.5}$ (units: μg m^{-3}) for 18 grids located in BTH. The correlation coefficient (R) and normalized mean bias (NMB; units: %) are also shown in (c−d). Here, R is the correlation coefficient between simulated and observed concentrations. NMB = $(\sum_{i=1}^{N}(M_i - O_i))/\sum_{i=1}^{N}O_i \times 100\%$, where O_i and M_i are the observed and simulated concentrations, respectively; i refers to the ith sample, and N is the total number of samples.

3.2 The relationships between atmospheric oxidants and T2/RH

255 The concentrations of total oxidant (O_x = O_3 + NO_2), hydroxyl radical (OH), and
256 nitrogen trioxide (NO_3) are usually used to characterize the atmospheric oxidation
257 capacity (Kang et al., 2021; Tang et al., 2022). Figures 2a−c and 2d−f show the boxplots
258 of simulated daily concentrations of O_x, OH, and NO_3 in T2 bins and in RH bins
259 (described in Sect. 2.2), respectively, considering the 18 grids of BTH in JJA of year
260 2019 (620 valid samples as also described in Sect. 2.2) from the CTRL simulation to
261 investigate the levels of atmospheric oxidation capacity under different temperature and
262 humidity conditions. The O_x and NO_3 concentrations gradually increased as T2 went up,
263 with the mean values increasing from 44.2 ppb and 5.0 × 10^{-3} ppb in the bin of ≤20℃ to
264 81.3 ppb and 3.3 × 10^{-2} ppb in the bin of >32℃, respectively. The concentrations of OH
265 exhibited continuous increases as T2 was above 24℃, and the mean value increased from
266 2.5 × 10^{6} molec. cm^{-3} at T2 of 24−26℃ to 3.3 × 10^{6} molec. cm^{-3} at >32℃. The
267 relationships between O_x/OH/NO_3 and T2 indicate that the atmospheric oxidation
268 capacity is stronger at higher temperature, which favors the formation of both secondary
269 inorganic and organic particulates (Feng et al., 2019). As for the relationships between
270 atmospheric oxidation capacity and RH, there was a small increasing trend in simulated
271 O_x concentrations as RH increased, with a peak value of 69.5 ppb as RH was 45−50%.
272 OH concentrations showed a W-shaped trend, with valleys occurring when RH values
273 were 35−40% and 50−55%. NO_3 concentrations had an overall decreasing trend as RH
274 increased.

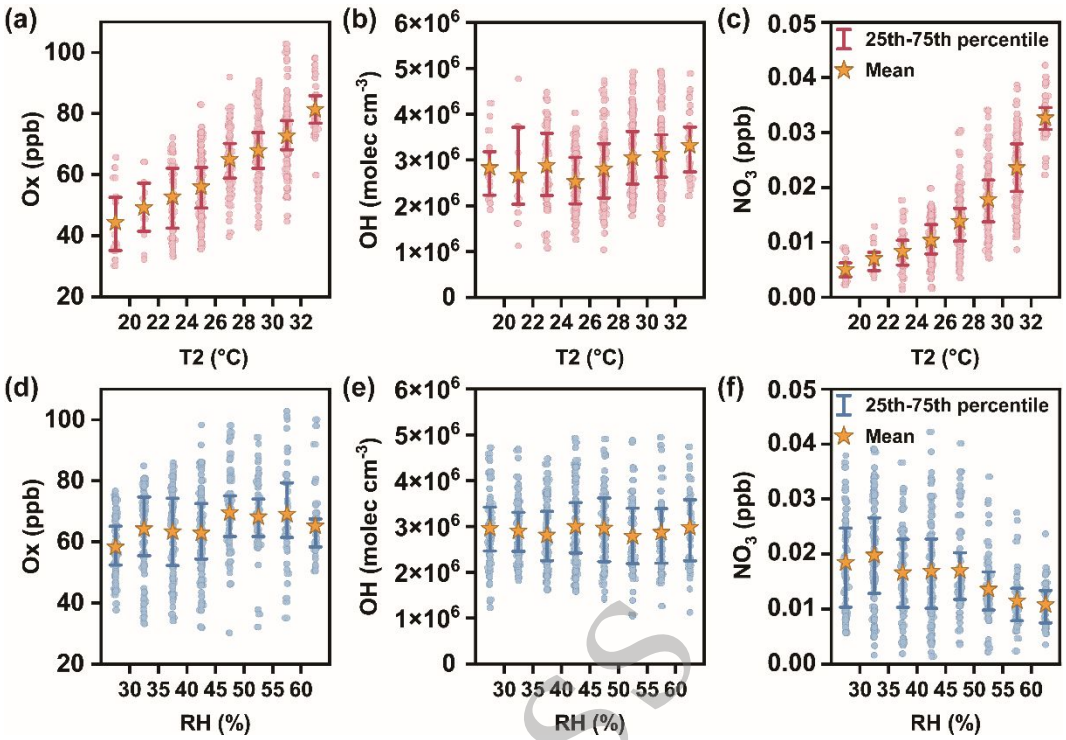

Fig. 2. The boxplots of surface-layer (a/d) total oxidant (O_x; units: ppb), (b/e) hydroxyl radical (OH; units: molec. cm^{-3}), and (c/f) nitrogen trioxide (NO_3; units: ppb) in each T2/RH bin in 18 grids of BTH in JJA of year 2019 (620 valid samples) from the CTRL simulation. T2 are binned to 2°C intervals and RH are binned to 5% intervals.

3.3 The relationships between air pollutants and T2/RH

3.3.1 The relationships between MDA8 O_3/$PM_{2.5}$ and T2/RH

Figure 3 displays the relationships between observed and simulated concentrations of MDA8 O_3 and T2/RH in BTH during JJA in 2019 (620 valid samples as described in Sect. 2.2). Both observed and simulated MDA8 O_3 increased as T2 went up, with increasing rates of 4.8 ppb °C^{-1} and 3.2 ppb °C^{-1}, respectively. As RH increased, there was a bimodal feature in observed and simulated MDA8 O_3 concentrations, with the peaks appearing as RH values were 30−35% and 45−50% for observations (30−35% and

55−60% for model results). Both observed and simulated MDA8 O_3 concentrations decreased as RH was greater than 60%. Compared to 55–60%, the net chemical production of O_3 had smaller positive values in the lower troposphere at RH>60% (Fig. 6c). In addition, the concentration of BC (a chemically inert species) also showed a drop as RH was above 60% (Fig. 4j), indicating that physical processes also contributed to the decrease in pollutant concentrations.

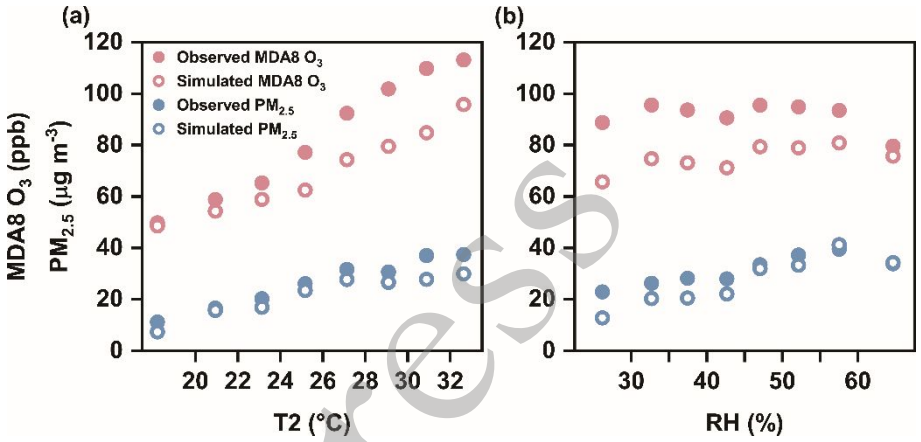

Fig. 3. Relationships between observed (solid dots) and simulated (hollow dots) MDA8 O_3 (pink dots)/$PM_{2.5}$ (blue dots) and (a) T2/(b) RH in 18 grids of BTH in JJA of 2019 (620 valid samples). Dots represent the mean of the daily concentrations of MDA8 O_3 (units: ppb) and $PM_{2.5}$ (units: μg m^{-3}) (a) versus daily T2 (units: °C) in each T2 bin and (b) versus daily RH (units: %) in each RH bin. T2 are binned to 2°C intervals and RH are binned to 5% intervals.

The relationships between observed and simulated concentrations of $PM_{2.5}$ and T2/RH in BTH during JJA in 2019 were also shown in Fig. 3. On the whole, concentrations of observed (simulated) $PM_{2.5}$ also increased as T2 rose, with linear trends of 1.9 (1.5) μg m^{-3} $℃^{-1}$. $PM_{2.5}$ concentrations exhibited fast increases as T2 was between ≤20℃ and 26−28℃ but had a small drop as T2 was between 28−30℃ and remained

306 relatively stable as T2 was >30℃. As RH increased from ≤30% to 55−60%, observed and
307 simulated $PM_{2.5}$ concentrations continuously increased. Same as MDA8 O_3, $PM_{2.5}$
308 concentrations decreased significantly as RH was above 60%. At 1005–913 hPa, net
309 chemical productions of $PM_{2.5}$ had larger values at RH>60% than those in the previous
310 humidity interval (Fig. 6d), so the physical processes dominated the drop of $PM_{2.5}$ at
311 RH>60%, as again indicated by the drop of BC concentration. The model generally
312 captures the variations in the observed MDA8 O_3/$PM_{2.5}$ with T2/RH.

313 *3.3.2 The relationships between $PM_{2.5}$ components and T2/RH*

314 Figures 4a−e and 4f−i show the simulated surface concentrations of $PM_{2.5}$
315 components (BC, SO_4^{2-}, NO_3^-, NH_4^+, and SOA) and the vertical distributions of
316 concentrations of SO_4^{2-}, NO_3^-, NH_4^+, and total nitrate ($NO_3^T = HNO_3 + NO_3^-$),
317 respectively, in T2 bins over BTH during JJA of year 2019 from the CTRL simulation.
318 The concentrations are averaged over the 18 grids in BTH. As T2 increased, the mean
319 concentrations of BC had a general upward trend. Since BC is assumed to be chemically
320 inert in the model (Dang and Liao, 2019), changes in BC concentrations can represent the
321 changes in pollutant concentrations by physical processes. The relationship between BC
322 and T2 indicates that physical processes were generally more conducive to the
323 accumulation of pollutants at higher temperature. To identify the contributions of
324 chemical processes to concentrations under different temperatures, the vertical profiles of
325 net chemical production of SO_4^{2-}, NO_3^-, and NH_4^+ in each T2 bin in 18 grids of BTH
326 during JJA of year 2019 are shown in Figs. 5a−c. In the lower troposphere (from the
327 surface to about 700 hPa altitude), the chemical production of SO_4^{2-} gradually increased
328 when T2 increased (Fig. 5a), consistent with the trends of atmospheric oxidants (Figs.

329 2a−c). Therefore, both physical and chemical processes contributed to the increases in
330 SO_4^{2-} concentrations as T2 increased (Fig. 4b).

331 For the formation of total nitrate, NO_2 oxidation by OH by $NO_2 + OH + M \rightarrow$
332 $HNO_3 + M$ is the major pathway during daytime, and the major reactions at nighttime
333 are $NO + O_3 \rightarrow NO_2 + O_2$, $NO_2 + O_3 \rightarrow NO_3 + O_2$, $NO_2 + NO_3 + M \rightarrow N_2O_5 + M$,
334 and $N_2O_5 + H_2O \rightarrow 2HNO_3$ (Dong et al., 2014; Leung et al., 2020). Higher
335 concentrations of NO_3^T at higher temperature (Fig. 4i) also confirms the enhancement of
336 atmospheric oxidation capacity. However, the variation of NO_3^- concentrations with T2
337 differed from that of NO_3^T. The surface concentration of NO_3^- at T2 of 22−24°C was
338 lower than that at 20−22°C (Fig. 4c) due to the larger negative net chemical productions
339 from the surface to 913 hPa at 22−24°C (Fig. 5b). Similarly, relative to 26−28°C, the net
340 chemical production of NO_3^- had lager negative values from the surface to 913 hPa and
341 consequently surface NO_3^- had lower concentration at T2 of 28−30°C. At 959–898 hPa,
342 the net chemical productions of NO_3^- were more negative both at 30−32°C and at >32°C
343 than those in the previous temperature interval, resulting in the decreases in NO_3^-
344 concentrations as T2 increased. Overall, in the lower troposphere, the lower
345 concentrations of NO_3^- at higher T2 were attributed to the evaporation of NO_3^-. For
346 NH_4^+, as a result of the larger negative net chemical productions from the surface to 913
347 hPa at 28−32°C (Fig. 5c), concentrations at 28−32°C were lower than those at 26−28°C
348 (Fig. 4d).

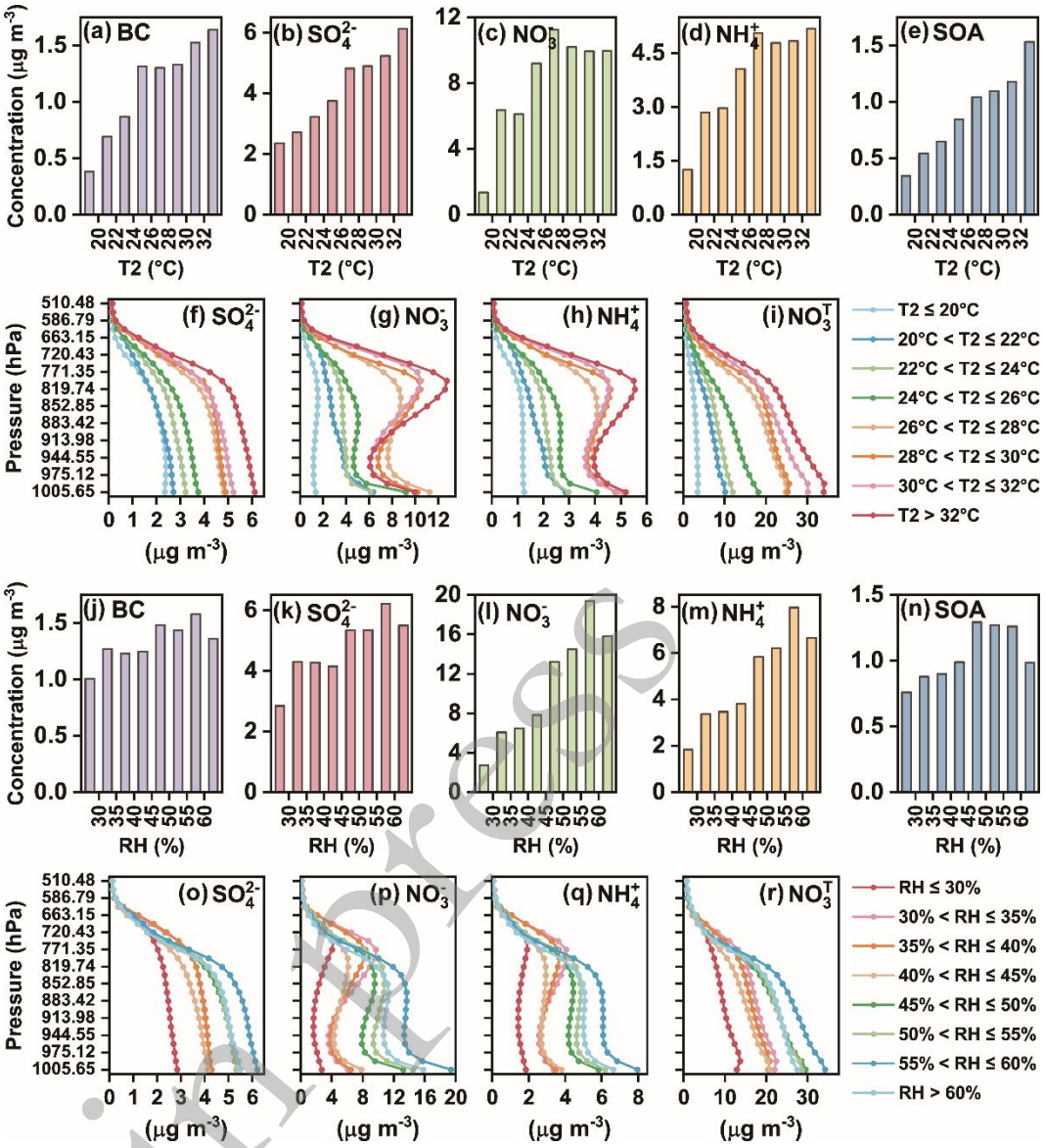

Fig. 4. (a–e/j–n) The surface concentrations (units: μg m^{-3}) of $PM_{2.5}$ components (BC, SO_4^{2-}, NO_3^-, NH_4^+, and SOA) and (f–i/o–r) the vertical distributions of concentrations (units: μg m^{-3}) of SO_4^{2-}, NO_3^-, NH_4^+, and total nitrate (NO_3^T = HNO_3 + NO_3^-) averaged over each T2/RH bin in 18 grids of BTH in JJA of year 2019 (620 valid samples) from the CTRL simulation.

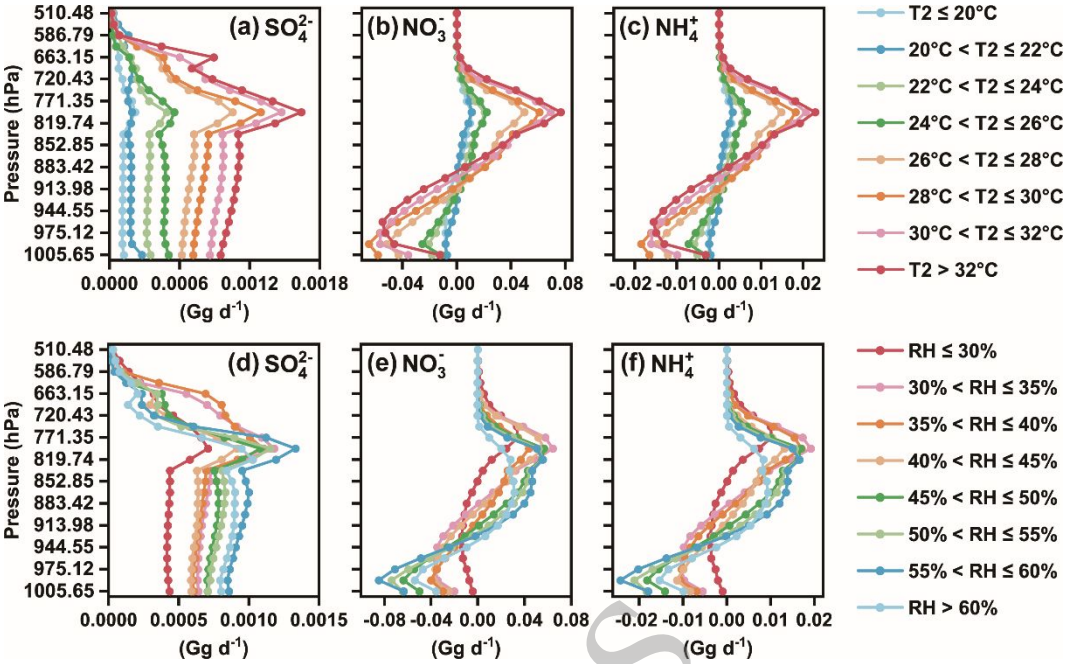

Fig. 5. The vertical profiles of net chemical production (units: Gg d^{-1}) of (a/d) SO_4^{2-}, (b/e) NO_3^-, and (c/f) NH_4^+ in each T2/RH bin in 18 grids of BTH in JJA of year 2019 (620 valid samples) from the CTRL simulation.

High temperature promotes the evaporation of SOA and the emission of biogenic VOCs (Lee et al., 2011; Liu et al., 2019; Wu et al., 2020). The significant upward trend in SOA concentrations indicates the dominant roles of the elevated levels of biogenic VOCs emissions and the enhanced atmospheric oxidation capacity as T2 went up. Simulated SOA concentrations were the lowest among all secondary aerosols, so it should not drive the trend of changes in $PM_{2.5}$ with T2.

The simulated surface and vertical concentrations of $PM_{2.5}$ components in RH bins in BTH during JJA of 2019 are presented in Figs. 4j−r, and the change in net chemical production of secondary inorganic components with RH is presented in Figs. 5d−f. As RH increased, the mean concentrations of BC showed a fluctuating upward trend and a large drop as RH was above 60%, with three peaks appearing at 30−35%, 45−50%, and

55−60% (Fig. 4j). SO_4^{2-} concentrations mimicked the variations in BC to some extent. Different from the changes in SO_4^{2-} concentrations, the concentrations of NO_3^- gradually increased with RH when RH was below 60%, and the changes in NH_4^+ followed that of NO_3^- (Figs. 4l−m). For SOA, the concentration increased first and then decreased as RH went up, with a peak concentration of 1.3 μg m^{-3} occurring when RH was 45−50%. Consistent with BC, concentrations of $PM_{2.5}$ secondary components showed a significant drop at RH of >60%, indicating the role of physical process. With respect to the role of chemical process, the net chemical production of SO_4^{2-} generally increased with RH, whereas that of NO_3^- and NH_4^+ had larger net loss at higher RH (Figs. 5d−f).

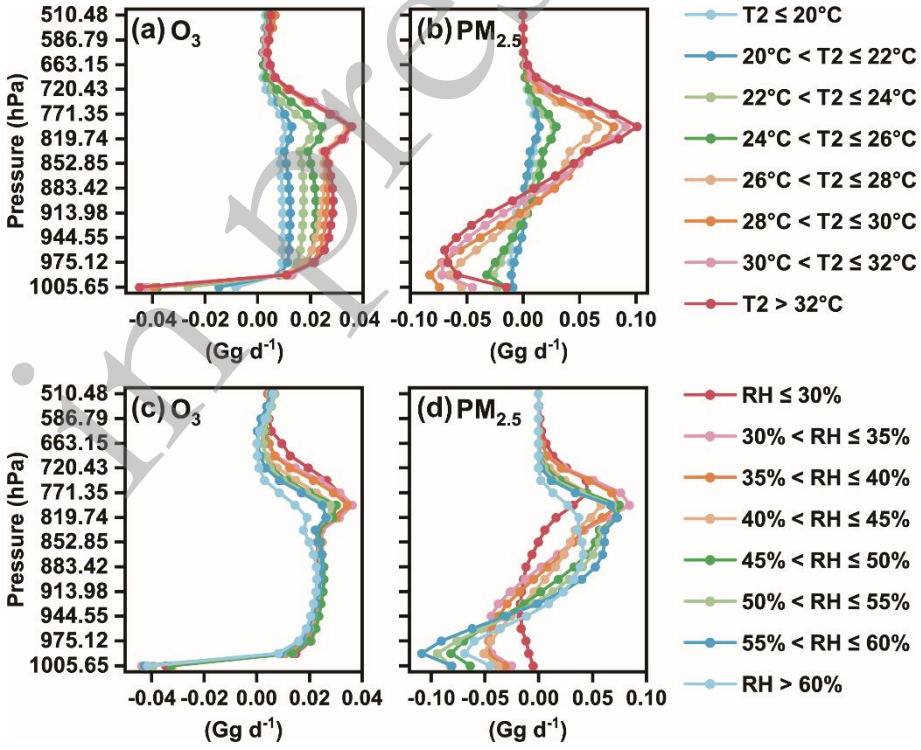

Fig. 6. Same as Fig. 5, but for (a/c) O_3 and (b/d) $PM_{2.5}$.

3.4 Impact of precursor emission reductions under different T2 and RH conditions

383 *3.4.1 Impact of precursor emission reductions on atmospheric oxidants*

384 Six numerical experiments (VOCs_10, VOCs_30, VOCs_50, NO_x_10+VOCs_10,
385 NO_x_10+VOCs_30, and NO_x_10+VOCs_50) were conducted to quantify the impacts of
386 different proportions of precursor emissions reduction in summer of 2019 on O_3 and
387 $PM_{2.5}$ in the BTH region under different temperature and humidity conditions. Figures
388 7a−d and 7e−h show the mean changes (Δ) of OH, O_3, NO_3, and sulfur oxidation ratio
389 (SOR = $n\text{-}SO_4^{2-}$ / ($n\text{-}SO_4^{2-}$ + $n\text{-}SO_2$), where $n\text{-}SO_4^{2-}$ and $n\text{-}SO_2$ are the molar
390 concentrations of SO_4^{2-} and SO_2, respectively) in T2 bins and in RH bins, respectively,
391 relative to the CTRL simulation. SOR is used to quantify the conversion degrees of sulfur
392 (Zhu et al., 2019).

393 The main sources of OH radical in urban areas are produced by the photolysis of O_3,
394 formaldehyde (HCHO) and nitrous acid (HONO), and the main sink of OH is to react
395 with NO_x, VOCs and peroxy radicals (HO_2) (Li et al., 2021; Dai et al., 2024).
396 Concentrations of OH mostly increased in the sensitivity simulations with emissions
397 reductions relative to the CTRL simulation. Further investigation showed that in cases of
398 reducing VOCs emissions alone, the increase in OH concentration was mainly driven by
399 the enhancement of photolysis of HONO, while in cases of simultaneously reducing NO_x
400 and VOCs emissions, it was mainly attributed to the weakening of the removal reaction
401 with NO_2. As T2 increased, ΔOH concentrations peaked at 20−22℃ in cases with
402 reductions of VOCs emissions alone and peaked at 24−26℃ in cases with reductions of
403 both VOCs and NO_x emissions, with the largest reduction of NO_x in this interval (Fig.
404 13a). ΔOH concentrations had a maximum value at RH of 45−50% except for the cases
405 of NO_x_10+VOCs_10 and NO_x_10+VOCs_30 simulations, which peaked at >60%. ΔOH

was larger as the percentage reduction of VOCs was higher. Compared to the cases with reductions of VOCs emissions alone, simultaneous reductions of NO_x and VOCs promoted the formation of OH radical when T2 was above 24℃ and in almost each RH interval.

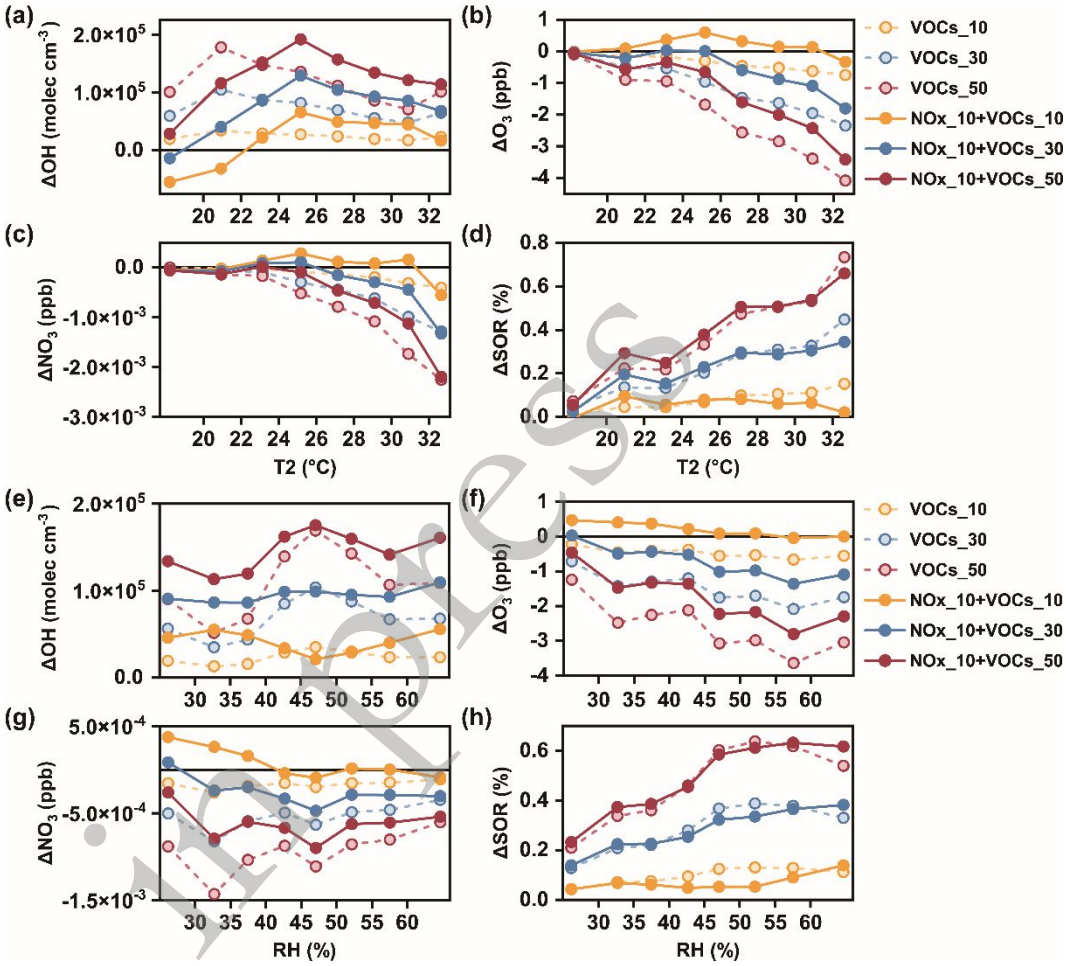

Fig. 7. Simulated mean changes in surface-layer (a/e) OH (units: molec. cm^{-3}), (b/f) O_3 (units: ppb), (c/g) NO_3 (units: ppb), and (d/h) sulfur oxidation ratio (SOR; units: %) in each T2/RH bin in 18 grids of BTH in JJA of 2019 (620 valid samples) in simulations with reductions of anthropogenic VOCs emissions alone (dotted lines with hollow dots) and simulations with simultaneous reductions of anthropogenic NO_x and VOCs emissions (solid lines with solid dots) relative to the CTRL simulation.

Concentrations of O_3 and NO_3 mostly decreased in the sensitivity simulations relative to the CTRL simulation. ΔO_3 and ΔNO_3 had larger negative values when T2 increased in all six simulations. When RH was lower than 60%, ΔO_3 had larger negative values as RH increased. The highest reductions in NO_3 concentrations occurred at RH of 30−35% (45−50%) in cases with reductions of VOCs emissions alone (of both VOCs and NO_x emissions). The larger the percentage reduction of VOCs emissions, the higher the decreases in O_3 and NO_3. Reducing both NO_x and VOCs emissions suppressed the decreases in O_3 and NO_3 concentrations relative to reducing VOCs emissions alone.

ΔSOR was generally positive in the sensitivity simulations relative to the CTRL simulation. ΔSOR increased when T2 went up except for the case of NO_x_10+VOCs_10, in which the highest increase occurred at 20−22℃. The maximum ΔSOR occurred as RH was 50−55% (above 55%) in cases with reductions of VOCs emissions alone (of both NO_x and VOCs emissions). The simulation with larger reduction of VOCs emissions led to the higher increase in SOR.

3.4.2 Impact of precursor emission reductions on MDA8 O_3 concentrations

The absolute and percentage changes in MDA8 O_3 concentrations in each T2 and RH intervals in BTH in JJA of 2019 with the six emission reduction measures are summarized in Fig. 8. The changes in mean MDA8 O_3 concentrations were always negative. As T2 went up, the absolute values of ΔMDA8 O_3 gradually increased, with maximum values of 0.9, 2.7, 4.7, 3.4, and 5.2 ppb in simulations of VOCs_10, VOCs_30, VOCs_50, NO_x_10+VOCs_30, and NO_x_10+VOCs_50, respectively. In the NO_x_10+VOCs_10 simulation, although the decreases in MDA8 O_3 concentrations did not increase monotonically with T2, the decreases in the 75th percentile of MDA8 O_3 did

(Fig. 9). As for the percentage changes in MDA8 O_3, NO_x_10+VOCs_10, NO_x_10+VOCs_30, and NO_x_10+VOCs_50 simulations had the lowest values (−1.7%, −3.5%, and −5.4%, respectively) at T2 of >32℃, while VOCs_10, VOCs_30, and VOCs_50 simulations exhibited the lowest values (−0.9%, −2.8%, and −4.9%, respectively) at 30−32℃. When RH increased, the absolute and percentage decreases of MDA8 O_3 concentrations both exhibited a bimodal trend, with the peaks appearing at RH of 30−35% and 45−50% in the NO_x_10+VOCs_10 simulation and at 30−35% and 55−60% in other simulations. The highest reductions were simulated to be 0.8 (1.0%), 2.6 (3.1%), 4.6 (5.4%), 1.0 (1.2%), 2.7 (3.1%), and 4.5 ppb (5.2%) in VOCs_10, VOCs_30, VOCs_50, NO_x_10+VOCs_10, NO_x_10+VOCs_30, and NO_x_10+VOCs_50 simulations, respectively.

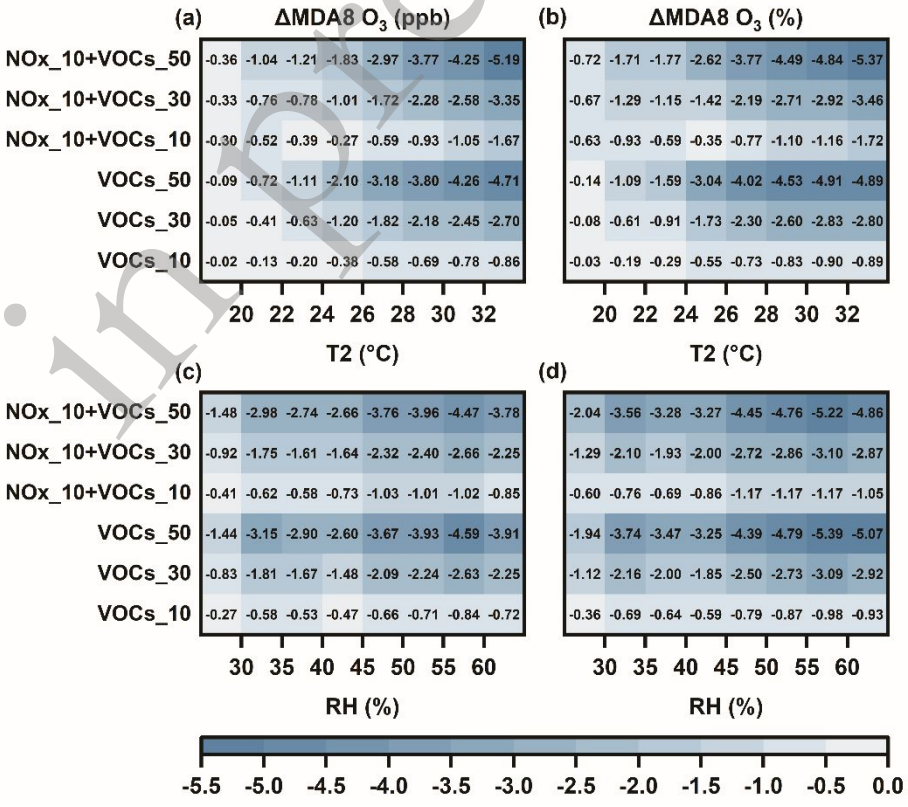

Fig. 8. (a)/(c) Absolute (units: ppb) and (b)/(d) percentage changes (units: %) in MDA8 O_3 concentrations in each T2 and bins in 18 grids of BTH in JJA of 2019 (620 valid samples) in VOCs_10, VOCs_30, VOCs_50, NO_x_10+VOCs_10, NO_x_10+VOCs_30, and NO_x_10+VOCs_50 simulations (from bottom to top) relative to the CTRL simulation.

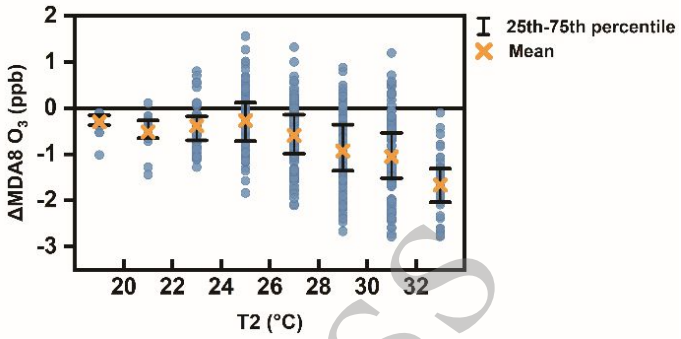

Fig. 9. The boxplots of absolute changes (units: ppb) in MDA8 O_3 concentrations in each T2 bin in 18 grids of BTH in JJA of 2019 for all valid samples in the NO_x_10+VOCs_10 simulation relative to the CTRL simulation.

In summary, implementing precursor emission reductions can effectively mitigate summer O_3 pollution in BTH, especially in the case with the higher reduction of VOCs emissions. Furthermore, relative to the situations in RH intervals, a larger reduction of VOCs emissions at higher T2 (>30℃) showed better effectiveness of controlling O_3 pollution.

3.4.3 Impact of precursor emission reductions on $PM_{2.5}$ concentrations

Figure 10 shows the absolute and percentage changes in $PM_{2.5}$ concentrations under different temperature and humidity conditions in JJA of 2019 in 18 grids of BTH resulting from emission reductions. By reducing VOCs emissions, the highest and second largest values of $\Delta PM_{2.5}$ concentrations occurred as T2 was above 32℃ and was

471 26−28℃, respectively. With simultaneous reductions in NO_x and VOCs emissions, the
472 absolute and percentage reductions in $PM_{2.5}$ mostly became larger as T2 increased. The
473 highest reductions in mean concentrations were 1.1 (3.5%), 1.0 (3.3%), and 0.9 μg m^{-3}
474 (3.0%) in the bin of >32 ℃ in cases of NO_x_10+VOCs_10, NO_x_10+VOCs_30, and
475 NO_x_10+VOCs_50 simulations, respectively.

476 Reducing 10% of NO_x emissions with 10%, 30%, and 50% of VOCs emissions were
477 simulated to result in the highest reductions of 1.6, 1.4, and 1.2 μg m^{-3}, respectively, in
478 mean concentrations of $PM_{2.5}$ in the bin of 55−60%. The simulated largest percentage
479 decreases in mean $PM_{2.5}$ concentrations occurred as RH was above 60%, with values of
480 3.7%, 3.2%, and 2.8% in NO_x_10+VOCs_10, NO_x_10+VOCs_30, and
481 NO_x_10+VOCs_50 simulations, respectively.

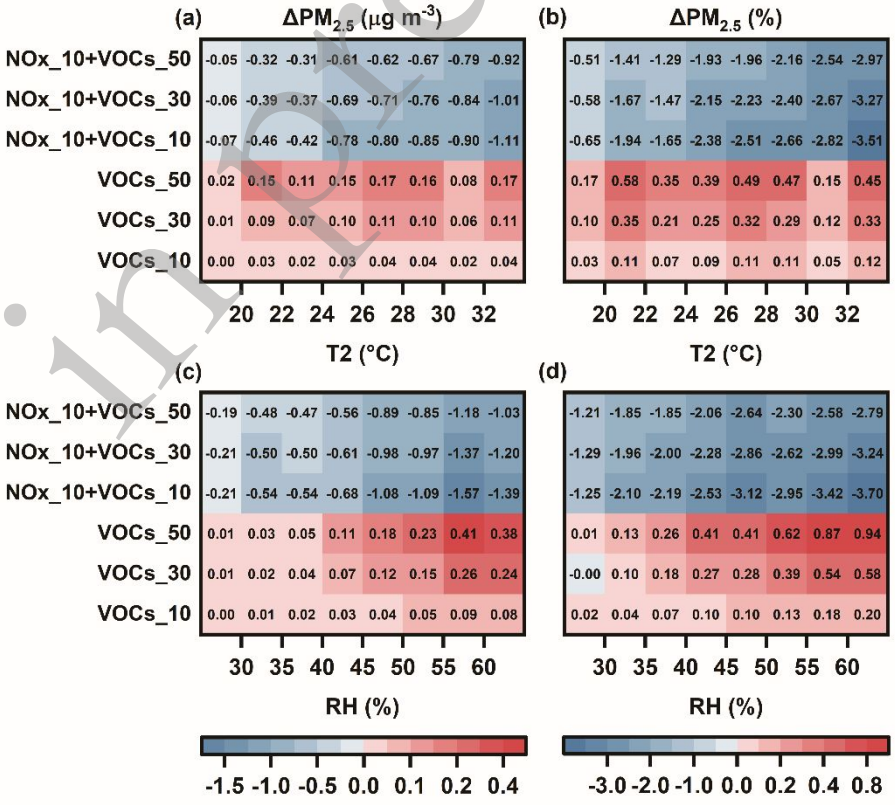

482

483 **Fig. 10.** Same as Fig. 8, but for $PM_{2.5}$. The unit of absolute change is μg m^{-3}.

484 It was obviously shown that simultaneous reductions in NO_x and VOCs emissions
485 could alleviate $PM_{2.5}$ pollution, but reductions in VOCs emissions alone exacerbated
486 $PM_{2.5}$ pollution. Reducing a smaller proportion of VOCs emissions resulted in a smaller
487 increase in $PM_{2.5}$ concentrations in cases of reducing VOCs emissions alone and a larger
488 decrease in cases of simultaneously reducing NO_x and VOCs emissions. As RH was
489 above 55%, the control measures on VOCs emissions were simulated to lead to the
490 highest decreases in $PM_{2.5}$.

491 *3.4.4 Impact of precursor emission reductions on $PM_{2.5}$ component concentrations*

492 The absolute and percentage changes in secondary components of $PM_{2.5}$ in each T2
493 and RH bins are presented in Figs. 11 and 12, respectively.

494 3.4.4.1 SOA

495 All of the six emission reduction measures led to reductions in SOA concentrations.
496 As T2 increased, the reductions in mean SOA concentrations became larger, consistent
497 with the reductions in O_3 and NO_3 concentrations (Figs. 7b−c), with the highest
498 reductions of 4.6×10^{-2} (3.0%), 0.1 (8.8%), 0.2 (14.5%), 3.3×10^{-2} (2.1%), 0.1 (8.1%),
499 and 0.2 μg m^{-3} (14.0%) in simulations of VOCs_10, VOCs_30, VOCs_50,
500 NO_x_10+VOCs_10, NO_x_10+VOCs_30, and NO_x_10+VOCs_50, respectively. With
501 respect to the results in RH intervals, the maximum absolute (percentage) decreases in
502 mean SOA concentrations of 2.9×10^{-2}–0.2 μg m^{-3} (2.1%−15.8%) occurred at RH of
503 55−60% (above 60%), when the average concentrations of O_3 had the highest (second
504 highest) declines (Fig. 7f). Compared to the cases with reductions in both NO_x and VOCs
505 emissions, reducing VOCs emissions alone resulted in greater reductions in SOA

506 concentration due to the larger decreases in O_3 and NO_3 as well as the smaller increases
507 in OH (Fig. 7).

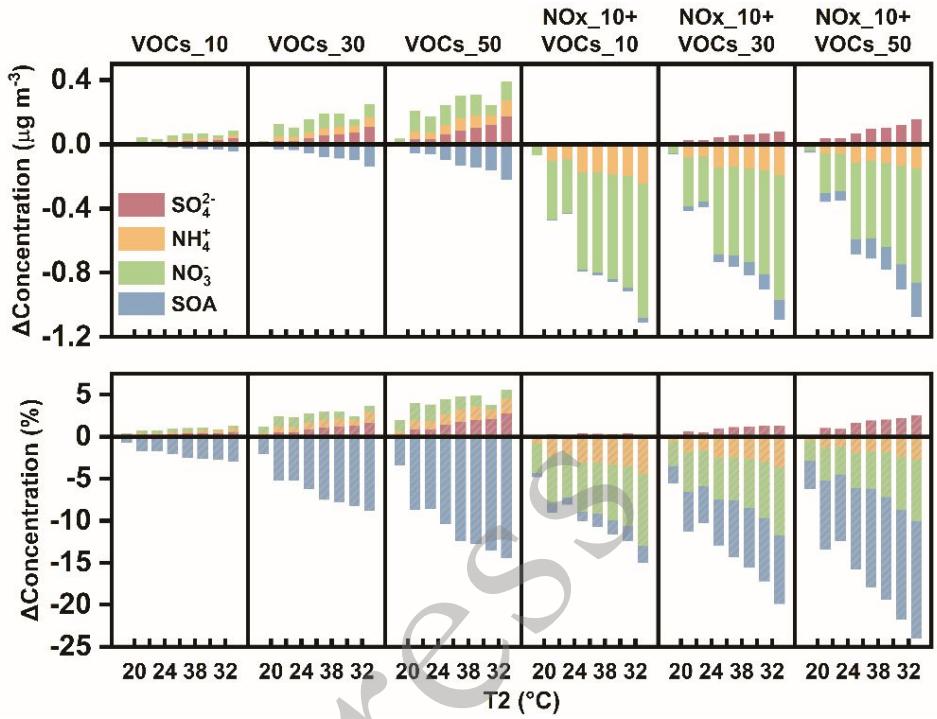

508

509 **Fig. 11.** Absolute (units: μg m^{-3}) and percentage changes (units: %) in concentrations of
510 $PM_{2.5}$ secondary components (SO_4^{2-}, NO_3^-, NH_4^+, and SOA) in each T2 bin in 18 grids
511 of BTH in JJA of 2019 (620 valid samples) in VOCs_10, VOCs_30, VOCs_50,
512 NO_x_10+VOCs_10, NO_x_10+VOCs_30, and NO_x_10+VOCs_50 simulations (from left
513 to right) relative to the CTRL simulation.

514 3.4.4.2 Sulfate

515 In contrast to SOA, six emission reduction measures all promoted the increases in
516 SO_4^{2-}. Controlling the emissions of NO_x and VOCs led to the increases in OH radical
517 (Figs. 7a and 7e), which enhanced the gas-phase oxidation of SO_2 and resulted in the
518 increases in SO_4^{2-}. Both the absolute and percentage increases of SO_4^{2-} concentrations
519 gradually increased as T2 went up, with the maximum of 3.6 × 10^{-2}–0.2 μg m^{-3} and

0.6%−2.7%, respectively, except for the NO_x_10+VOCs_10 simulation. In the five cases mentioned above, the positive changes of SOR were highest as T2 was above 32℃ (Fig. 7d). In the NO_x_10+VOCs_10 simulation, the highest absolute (percentage) increases occurred as T2 was 26−28℃ (24−26℃), when the increase in OH radical was second highest (highest) (Fig. 7a). In cases with reductions of VOCs emissions alone (both NO_x and VOCs emissions), the highest absolute and percentage increases in increased SO_4^{2-} concentrations occurred at RH of 50−60% (>55%), consistent with the changes in SOR (Fig. 7h). In each T2 and RH bins, the absolute (percentage) increases in SO_4^{2-} were positively correlated with the percentage reduction of VOCs emissions.

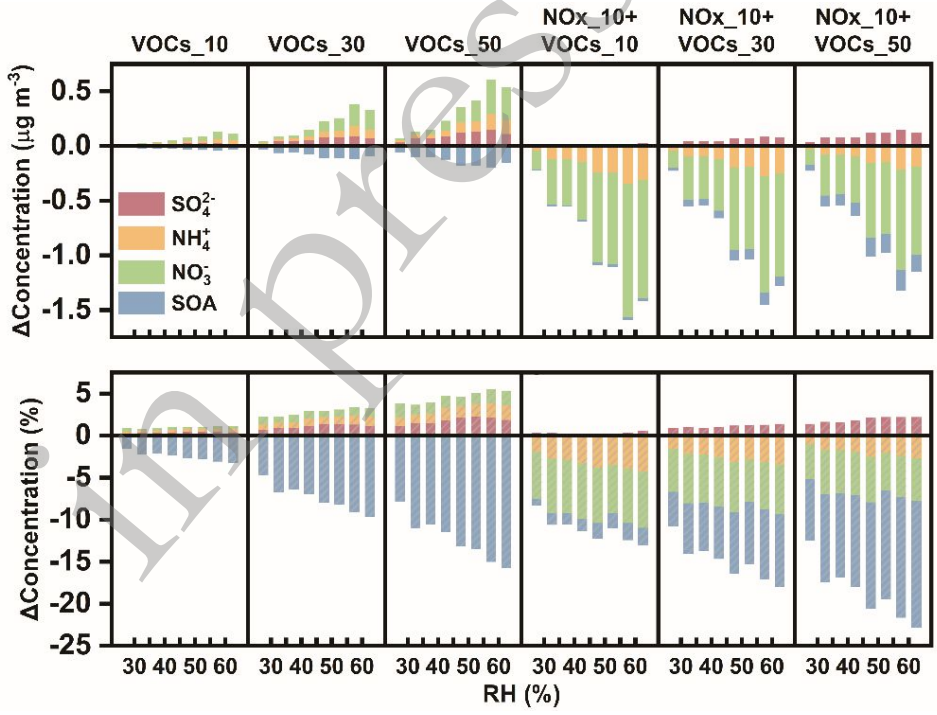

Fig. 12. Same as Fig. 11, but for each RH bin.

3.4.4.3 Nitrate

In the simulations with reductions of VOCs emissions alone, the higher proportion of VOCs reduction, the larger the increase in NO_3^- concentration. The increases of OH

534 radical promoted the formation of HNO_3 during daytime, while the formation of HNO_3 at
535 nighttime through hydrolysis was reduced due to lower N_2O_5 from the decreases in O_3.
536 The daily concentrations of NO_3^T increased as shown in Figs. 13b and 13e. Sulfate and
537 nitrate compete for NH_3, so the enhanced SO_4^{2-} formation consumed more NH_3,
538 resulting in a decrease in the proportion allocated to the particle phase in NO_3^T (as shown
539 in nitrate particle fraction ($\varepsilon(NO_3^-) = n\text{-}NO_3^- / (n\text{-}HNO_3 + n\text{-}NO_3^-)$ in Figs. 13c and
540 13f). However, since NO_3^T was increased, there was still slight increase in daily
541 concentration of NO_3^-. Average over each T2 bin, the highest absolute (percentage)
542 increases in NO_3^- concentrations occurred as T2 was 26−28℃ (20−24℃), with values of
543 3.2×10^{-2} (0.4%), 9.1×10^{-2} (1.2%), and 0.1 μg m^{-3} (2.0%) in VOCs_10, VOCs_30,
544 VOCs_50 simulations relative to the CTRL simulation, respectively. As T2 was 20−22℃
545 and 22−24℃, the increases in OH radical were highest and second highest, respectively
546 (Fig. 7a), leading to large formation of HNO_3 and NO_3^-. As for each RH interval, the
547 highest absolute (percentage) increases occurred when RH was 55−60% (above 60%),
548 with values of 6.8×10^{-2}–0.3 μg m^{-3} (0.4%−1.7%).

549 With simultaneous reductions in NO_x and VOCs emissions, the daytime and
550 nighttime formation of HNO_3 both slowed down due to the reductions in NO_x and O_3
551 concentrations, inhibiting the generation of NO_3^T and leading to the decreases in daily
552 concentrations of NO_3^-. The smaller proportion of VOCs reduction resulted in the larger
553 decreases in NO_3^- concentrations due to the smaller increases in OH (Figs. 7a and 7e)
554 and the larger decreases in NO_x (Figs. 13a and 13d), which inhibited both daytime and
555 nighttime HNO_3 formation more significantly. As T2 went up, the reductions in mean
556 NO_3^- concentration exhibited higher efficiency (larger reductions), consistent with the

reductions in O_3 and NO_3 concentrations (Figs. 7b–c). The highest reductions were simulated to be 0.8 (8.5%), 0.8 (8.1%), 0.7 μg m^{-3} (7.3%) in simulations of NO_x_10+VOCs_10, NO_x_10+VOCs_30, and NO_x_10+VOCs_50, respectively. Average over each RH bin, the highest reductions in NO_3^- concentrations occurred when RH was 55–60% (the RH bin with the largest decrease in mean O_3 concentration), with values of 1.2, 1.1, and 0.9 μg m^{-3} in NO_x_10+VOCs_10, NO_x_10+VOCs_30, and NO_x_10+VOCs_50 simulations relative to the CTRL simulation, respectively.

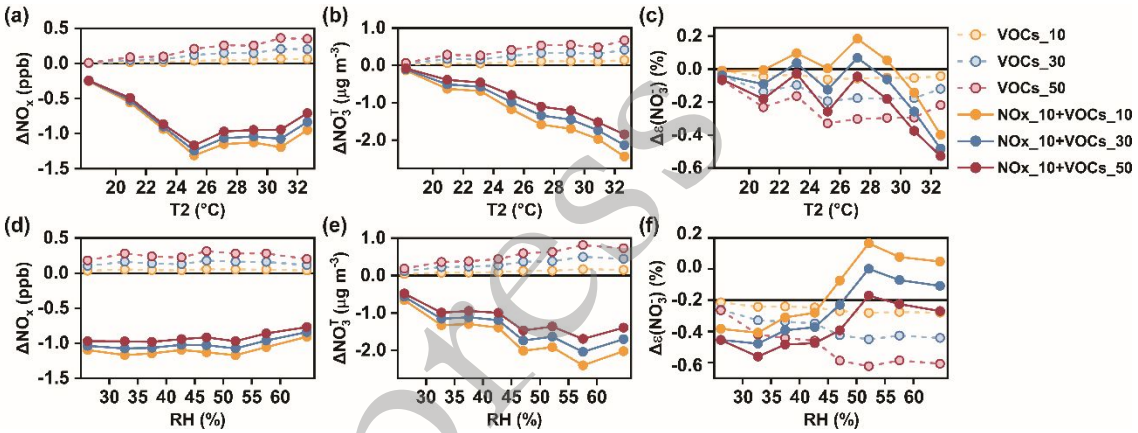

Fig. 13. Same as Fig. 7, but for surface-layer (a/d) NO_x (units: ppb), (b/e) NO_3^T (units: μg m^{-3}), and (c/f) nitrate particle fraction ($\varepsilon(NO_3^-)$ = n-NO_3^- / (n-HNO_3 +n-NO_3^-); units: %).

3.4.4.4 Ammonium

The reductions in emissions of VOCs and NO_x affect the concentrations of NH_4^+ through the formation of SO_4^{2-} and NO_3^-. Reducing VOCs emissions alone (NO_x and VOCs emissions simultaneously) resulted in an increase (a decrease) in NH_4^+ concentrations. As T2 increased, the increases (decreases) in mean NH_4^+ concentrations became larger in both cases. The highest reductions in mean NH_4^+ concentrations were

574 simulated to be 0.1−0.2 μg m^{-3} (2.8%−4.5%) with the simultaneous reductions in NO_x
575 and VOCs emissions. For each RH interval, the highest absolute and percentage increases
576 (decreases) in mean NH_4^+ concentrations occurred when RH was 55−60% and was
577 above 60% in both cases, respectively.

578 Overall, simultaneously reducing NO_x and VOCs emissions alleviated $PM_{2.5}$
579 pollution effectively, especially with a smaller proportion of VOCs reduction. With
580 simultaneous reductions in NO_x and VOCs emissions, although there was a positive
581 correlation between the decrease in SOA concentrations and the percentage reduction of
582 VOCs emissions, the impact of SOA changes on the level of $PM_{2.5}$ was weak due to its
583 small proportion in $PM_{2.5}$. Smaller percentage reduction in VOCs resulted in the smaller
584 increase in SO_4^{2-} concentrations due to the smaller increase in OH radicals, and led to
585 the higher decrease in NO_3^- concentration owing to the larger reduction in both daytime
586 and nighttime formation of HNO_3 caused by the larger decrease in NO_x. At higher
587 temperatures, simultaneous reductions in NO_x and VOCs emissions generated more
588 sulfate but significantly suppressed the generation of SOA, nitrate, and ammonium due to
589 the larger decreases in O_3 and NO_3, leading to larger reductions in $PM_{2.5}$ concentrations.
590 When RH was above 55%, the absolute and percentage decreases in $PM_{2.5}$ concentrations
591 reached the maximum values, caused by the highest reductions in SOA, NO_3^-, and NH_4^+
592 concentrations due to the highest reduction in O_3 concentrations.

593 **4. Conclusions**

594 We used the observed hourly concentrations of O_3 and $PM_{2.5}$ from MEE,
595 meteorological parameters from MERRA-2, and the model results from the nested-grid
596 version of the GEOS-Chem model to examine the relationships between O_3, $PM_{2.5}$, and

597 $PM_{2.5}$ components and T2/RH over the BTH and to investigate the effectiveness of
598 precursor emission reductions on O_3 and $PM_{2.5}$ in BTH under different temperature and
599 humidity conditions in the summer of 2019.

600 Both observed (simulated) MDA8 O_3 and $PM_{2.5}$ concentrations were found to
601 increase as T2 went up, with linear trends of 4.8 (3.2) ppb ℃$^{-1}$ and 1.9 (1.5) μg m^{-3} ℃$^{-1}$,
602 respectively. Atmospheric oxidation capacity was stronger at higher temperature,
603 resulting in the increases in $PM_{2.5}$ secondary components. As RH increased,
604 concentrations of $PM_{2.5}$ secondary components increased first and then decreased. SOA
605 peaked at RH of 45−50% when O_x and NO_3 were at a high level, while SO_4^{2-}, NO_3^-, and
606 NH_4^+ peaked at RH of 55−60%. There was a bimodal trend in observed/simulated
607 MDA8 O_3 concentrations (peaking at 30−35% and 45−50%/30−35% and 55−60%). Both
608 observed and simulated $PM_{2.5}$ concentrations peaked at RH of 55−60%.

609 The results of the six sensitivity experiments showed that implementing precursor
610 emission reductions can effectively mitigate summer O_3 pollution in BTH. The larger the
611 percentage reductions of VOCs emissions, the larger the reductions in MDA8 O_3. As T2
612 went up, the absolute values of ΔMDA8 O_3 showed an overall increasing trend, with the
613 maximum values of 0.9−5.2 ppb at T2 of >32℃ in the six simulations. The percentage
614 reductions in MDA8 O_3 were the largest (0.9%−4.9%) at T2 of 30−32℃ with reductions
615 in VOCs emissions alone and (1.7%−5.4%) at T2 of >32℃ with simultaneous reductions
616 in NO_x and VOCs. When RH increased, the decreases of MDA8 O_3 concentrations
617 exhibited a bimodal trend. Among the six simulations, the largest decreases in MDA8 O_3
618 (4.6 ppb (5.4%)) occurred at RH of 55−60% with a 50% reduction in VOCs emissions.

Different from the responses of O_3, reducing VOCs emissions alone exacerbated $PM_{2.5}$ pollution. Simultaneous reductions in NO_x and VOCs emissions alleviated summer $PM_{2.5}$ pollution in BTH. Reducing a smaller proportion of VOCs resulted in a larger decrease in $PM_{2.5}$ concentration, driven by the larger decrease in NO_3^- concentration due to the larger reduction in both daytime and nighttime formation of HNO_3 from the larger decrease in NO_x. As T2 increased, reductions in $PM_{2.5}$ mostly became larger, with the peak values of 1.1 (3.5%), 1.0 (3.3%), and 0.9 μg m^{-3} (3.0%) at T2 of >32℃, respectively, in NO_x_10+VOCs_10, NO_x_10+VOCs_30, and NO_x_10+VOCs_50 simulations. When T2 was above 32℃, the reductions in SOA, NO_3^-, and NH_4^+ concentrations reached their maximum values owing to the large decreases in O_3 and NO_3. As for the RH intervals, the highest absolute reduction in $PM_{2.5}$ concentrations (1.2−1.6 μg m^{-3}) occurred at RH of 55−60% and the highest percentage reduction (2.8%−3.7%) occurred in the bin of >60% with simultaneous reductions in NO_x and VOCs. At RH of >55%, the large reductions in O_3 contributed to the large reductions in SOA, NO_3^-, and NH_4^+ concentrations.

In summary, reducing a larger proportion of VOCs emissions can lead to larger reduction in MDA8 O_3 in BTH during summer. The decreases in MDA8 O_3 caused by precursor emission reductions are more sensitive to T2 than to RH. Higher reduction of VOCs emissions at higher T2 is more effective for alleviating summer O_3 pollution in BTH. When $PM_{2.5}$ pollution is a concern in summer, NO_x reduction combined with a small proportion reduction of VOCs is the best measure. The reduction in $PM_{2.5}$ from reducing precursor emissions is more sensitive to RH than to T2, with the best efficiency

641 at high RH. For the control of co-pollution of O_3 and $PM_{2.5}$ in summer in BTH, precursor
642 emission reductions have the best effect in a hot and humid conditions.

643 ***Acknowledgments.*** This work was supported by the National Natural Science
644 Foundation of China (Grant No. 91744311).

645 **REFERENCES**

646 Alexander, B., R. J. Park, D. J. Jacob, Q. B. Li, R. M. Yantosca, J. Savarino, C. C. W.
647 Lee, and M. H. Thiemens, 2005: Sulfate formation in sea-salt aerosols: Constraints
648 from oxygen isotopes. *Journal of Geophysical Research: Atmospheres*, 110,
649 D10307, http://doi.org/10.1029/2004JD005659.

650 Bey, I., and Coauthors, 2001: Global modeling of tropospheric chemistry with
651 assimilated meteorology: Model description and evaluation. *Journal of Geophysical*
652 *Research: Atmospheres*, **106**, 23073−23095, http://doi.org/10.1029/2001jd000807.

653 Chen, L., J. Zhu, H. Liao, Y. Yang, and X. Yue, 2020: Meteorological influences on
654 $PM_{2.5}$ and O_3 trends and associated health burden since China's clean air actions.
655 *Science of the Total Environment,* **744**, 140837,
656 https://doi.org/10.1016/j.scitotenv.2020.140837.

657 Cooke, W. F., C. Liousse, H. Cachier, and J. Feichter., 1999: Construction of a 1° × 1°
658 fossil fuel emission data set for carbonaceous aerosol and implementation and
659 radiative impact in the ECHAM4 model. *Journal of Geophysical Research:*
660 *Atmospheres*, **104**, 22137−22162, http://doi.org/10.1029/1999JD900187.

661 Dai, H. B., H. Liao, K. Li, X. Yue, Y. Yang, J. Zhu, J. B. Jin, B. J. Li, and X. W. Jiang,
662 2023: Composited analyses of the chemical and physical characteristics of
663 co-polluted days by ozone and $PM_{2.5}$ over 2013–2020 in the Beijing–Tianjin–Hebei

region. *Atmospheric Chemistry and Physics*, **23**, 23−39, https://doi.org/10.5194/acp-23-23-2023.

Dai, H. B., H. Liao, Y. Wang, and J. Qian, 2024: Co-occurrence of ozone and $PM_{2.5}$ pollution in urban/non-urban areas in eastern China from 2013 to 2020: Roles of meteorology and anthropogenic emissions. *Science of the Total Environment*, **924**, 171687, https://doi.org/10.1016/j.scitotenv.2024.171687.

Dang, R. J., and H. Liao, 2019: Severe winter haze days in the Beijing–Tianjin–Hebei region from 1985 to 2017 and the roles of anthropogenic emissions and meteorology. *Atmospheric Chemistry and Physics*, **19**, 10801–10816, https://doi.org/10.5194/acp-19-10801-2019.

Dang, R. J., H. Liao, and Y. Fu, 2021: Quantifying the anthropogenic and meteorological influences on summertime surface ozone in China over 2012–2017. *Science of the Total Environment*, **754**, 142394, https://doi.org/10.1016/j.scitotenv.2020.142394.

Dawson, J. P., P. J. Adams, and S. N. Pandis, 2007: Sensitivity of $PM_{2.5}$ to climate in the Eastern US: a modeling case study. *Atmospheric Chemistry and Physics*, **7**, 4295–4309, https://doi.org/10.5194/acp-7-4295-2007.

Ding, D., J. Xing, S. X. Wang, Z. X. Dong, F. F. Zhang, S. C. Liu, and J. M. Hao, 2022: Optimization of a NO_x and VOC cooperative control strategy based on clean air benefits. *Environmental Science & Technology*, **56**, 739−749, https://doi.org/10.1021/acs.est.1c04201.

Dong, X.Y., J. Li, J. S. Fu, Y. Gao, K. Huang, and G. H. Zhang, 2014: Inorganic aerosols responses to emission changes in Yangtze River Delta, China. *Science of the Total Environment,* **481**, 522–532, https://doi.org/10.1016/j.scitotenv.2014.02.076.

687 Fairlie, T. D., D. J. Jacob, and R. J. Park, 2007: The impact of transpacific transport of
688 mineral dust in the United States. *Atmospheric Environment*, **41**, 1251−1266,
689 http://doi:10.1016/j.atmosenv.2006.09.048.
690 Feng, T., and Coauthors, 2019: Secondary organic aerosol enhanced by increasing
691 atmospheric oxidizing capacity in Beijing–Tianjin–Hebei (BTH), China.
692 *Atmospheric Chemistry and Physics*, **19**, 7429–7443,
693 https://doi.org/10.5194/acp-19-7429-2019.
694 Fu, Y., and H. Liao, 2014: Impacts of land use and land cover changes on biogenic
695 emissions of volatile organic compounds in China from the late 1980s to the
696 mid-2000s: implications for tropospheric ozone and secondary organic aerosol.
697 *Tellus B: Chemical and Physical Meteorology*, **66**, 24987,
698 http://dx.doi.org/10.3402/tellusb.v66.24987.
699 Gelaro, R., and Coauthors, 2017: The modern-era retrospective analysis for research and
700 applications, version 2 (MERRA-2). *Journal of Climate*, **30**, 5419−5454,
701 http://doi.org/10.1175/JCLI-D-16-0758.1.
702 Gong, C., Y. Wang, H. Liao, P. Y. Wang, J. B. Jin, and Z. W. Han, 2022: Future
703 co-occurrences of hot days and ozone-polluted days over China under scenarios of
704 shared socioeconomic pathways predicted through a machine-learning approach.
705 *Earth's Future*, **10**, e2022EF002671, https://doi.org/10.1029/2022EF002671.
706 Guenther, A. B., X. Jiang, C. L. Heald, T. Sakulyanontvittaya, T. Duhl, L. K. Emmons,
707 and X. Wang, 2012: The Model of Emissions of Gases and Aerosols from Nature
708 version 2.1 (MEGAN2.1): an extended and updated framework for modeling

biogenic emissions. *Geoscientific Model Development*, **5**, 1471–1492, https://doi.org/10.5194/gmd-5-1471-2012.

Jacob, D. J., and D. A. Winner, 2009: Effect of climate change on air quality. *Atmospheric Environment*, **43**, 51−63, http://doi.org/10.1016/j.atmosenv.2008.09.051.

Jo, D. S., R. J. Park, M. J. Kim, and D. V. Spracklen, 2013: Effects of chemical aging on global secondary organic aerosol using the volatility basis set approach. *Atmospheric Environment*, **81**, 230−244, http://dx.doi.org/10.1016/j.atmosenv.2013.08.055.

Johnson, C. E., W. J. Collins, D. S. Stevenson, and R. G. Derwent, 1999: Relative roles of climate and emissions changes on future tropospheric oxidant concentrations. *Journal of Geophysical Research: Atmospheres*, **104**, 18631−18645, https://doi.org/10.1029/1999jd900204.

Kang, M. J., J. Zhang, H. L. Zhang, and Q. Ying, 2021: On the Relevancy of observed ozone increase during COVID-19 lockdown to summertime ozone and $PM_{2.5}$ control policies in China. *Environmental Science & Technology Letters*, **8**, 289−294, https://doi.org/10.1021/acs.estlett.1c00036.

Kleeman, M. J., 2008: A preliminary assessment of the sensitivity of air quality in California to global change. *Climatic Change*, **87**, 273−292, http://doi.org/10.1007/s10584-007-9351-3.

Lee, B. H., J. R. Pierce, G. J. Engelhart, and S. N. Pandis, 2011: Volatility of secondary organic aerosol from the ozonolysis of monoterpenes. *Atmospheric Environment*, **45**, 2443−2452, https://doi.org/10.1016/j.atmosenv.2011.02.004.

731 Leung, D. M., and Coauthors, 2020: Wintertime particulate matter decrease buffered by
732 unfavorable chemical processes despite emissions reductions in China. *Geophysical*
733 *Research Letters*, **47**, e2020GL087721, https://doi.org/10.1029/2020GL087721.
734 Li, K., and Coauthors, 2019b: A two-pollutant strategy for improving ozone and
735 particulate air quality in China. *Nature Geoscience*, **12**, 906−910,
736 https://doi.org/10.1038/s41561-019-0464-x.
737 Li, K., and Coauthors, 2021: Ozone pollution in the North China Plain spreading into the
738 late-winter haze season. *Proceedings of the National Academy of Sciences of the*
739 *United States of America*, **118**, e2015797118,
740 https://doi.org/10.1073/pnas.2015797118.
741 Li, K., D. J. Jacob, H. Liao, L. Shen, Q. Zhang, and K. H. Bates, 2019a: Anthropogenic
742 drivers of 2013–2017 trends in summer surface ozone in China. *Proceedings of the*
743 *National Academy of Sciences of the United States of America*, **116**, 422–427,
744 https://doi.org/10.1073/pnas.1812168116.
745 Li, K., D. J. Jacob, L. Shen, X. Lu, I. De Smedt, and H. Liao, 2020: Increases in surface
746 ozone pollution in China from 2013 to 2019: anthropogenic and meteorological
747 influences. *Atmospheric Chemistry and Physics*, **20**, 11423−11433,
748 https://doi.org/10.5194/acp-20-11423-2020.
749 Liao, H., W. T. Chen, and J. H. Seinfeld, 2006: Role of climate change in global
750 predictions of future tropospheric ozone and aerosols. *Journal of Geophysical*
751 *Research: Atmospheres*, **111**, D12304, http://doi.org/10.1029/2005JD006852.
752 Liu, H., D. J. Jacob, I. Bey, and R. M. Yantosca, 2001: Constraints from ^{210}Pb and ^{7}Be on
753 wet deposition and transport in a global three-dimensional chemical tracer model

754 driven by assimilated meteorological fields. *Journal of Geophysical Research:*
755 *Atmospheres*, **106**, 12109−12128, http://doi.org/10.1029/2000jd900839.
756 Liu, S., and Coauthors, 2019: Climate-driven trends of biogenic volatile organic
757 compound emissions and their impacts on summertime ozone and secondary organic
758 aerosol in China in the 2050s. *Atmospheric Environment*, **218**, 117020,
759 https://doi.org/10.1016/j.atmosenv.2019.117020.
760 Luo, Y. H., and Coauthors, 2022: Seasonal changes in the recent decline of combined
761 high $PM_{2.5}$ and O_3 pollution and associated chemical and meteorological drivers in
762 the Beijing–Tianjin–Hebei region, China. *Science of the Total Environment*, **838**,
763 156312, http://dx.doi.org/10.1016/j.scitotenv.2022.156312.
764 Park, R. J., D. J. Jacob, B. D. Field, R. M. Yantosca, and M. Chin, 2004: Natural and
765 transboundary pollution influences on sulfate-nitrate-ammonium aerosols in the
766 United States: Implications for policy. *Journal of Geophysical Research:*
767 *Atmospheres*, **109**, D15204, http://doi.org/10.1029/2003JD004473.
768 Park, R. J., D. J. Jacob, M. Chin, and R. V. Martin, 2003: Sources of carbonaceous
769 aerosols over the United States and implications for natural visibility. *Journal of*
770 *Geophysical Research: Atmospheres*, **108**, D124355,
771 http://doi:10.1029/2002JD003190.
772 Pye, H. O. T., H. Liao, S. Wu, L. J. Mickley, D. J. Jacob, D. K. Henze, and J. H. Seinfeld,
773 2009: Effect of changes in climate and emissions on future sulfate-nitrate-ammonium
774 aerosol levels in the United States. *Journal of Geophysical Research: Atmospheres*,
775 **114**, D01205, http://doi.org/10.1029/2008JD010701.

776 Shah, V., and Coauthors, 2018: Chemical feedbacks weaken the wintertime response of
777 particulate sulfate and nitrate to emissions reductions over the eastern United States.
778 *Proceedings of the National Academy of Sciences of the United States of America*,
779 **115**, 8110–8115, https://doi.org/10.1073/pnas.1803295115.
780 Tang, M. X., and Coauthors, 2022: Decisive role of ozone formation control in winter
781 $PM_{2.5}$ mitigation in Shenzhen, China. *Environmental Pollution*, **301**, 119027,
782 https://doi.org/10.1016/j.envpol.2022.119027.
783 Wang, F., and Coauthors, 2022: Machine learning and theoretical analysis release the
784 non-linear relationship among ozone, secondary organic aerosol and volatile organic
785 compounds. *Journal Environment Science*, **114**, 75−84,
786 https://doi.org/10.1016/j.jes.2021.07.026.
787 Wang, X. L., 2024. Historical air quality data in China. available at:
788 https://quotsoft.net/air, last access: 15 February 2024.
789 Wang, Y. H., D. J. Jacob, and J. A. Logan, 1998: Global simulation of tropospheric
790 O_3-NO_x-hydrocarbon chemistry 1. Model formulation. *Journal of Geophysical*
791 *Research: Atmospheres*, **103**, 10713−10725, https://doi.org/10.1029/98jd00158.
792 Wang, Y., and H. Liao, 2020: Effect of emission control measures on ozone
793 concentrations in Hangzhou during G20 meeting in 2016. *Chemosphere*, **261**,
794 127729, https://doi.org/10.1016/j.chemosphere.2020.127729.
795 Wang, Y., Q.Q. Zhang, K. He, Q. Zhang, and L. Chai, 2013: Sulfate-nitrate-ammonium
796 aerosols over China: response to 2000–2015 emission changes of sulfur dioxide,
797 nitrogen oxides, and ammonia. *Atmospheric Chemistry and Physics*, **13**, 2635–2652,
798 https://doi.org/10.5194/acp-13-2635-2013 .

799 Wesely, M. L., 1989: Parameterization of surface resistances to gaseous dry deposition in
800 regional-scale numerical models. *Atmospheric Environment*, **23**, 1293−1304,
801 http://doi.org/10.1016/0004-6981(89)90153-4 .
802 Wu, K., and Coauthors, 2020: Estimation of biogenic VOC emissions and their
803 corresponding impact on ozone and secondary organic aerosol formation in China.
804 *Atmospheric Research*, **231**, 104656,
805 https://doi.org/10.1016/j.atmosres.2019.104656.
806 Xiang, S. L., and Coauthors, 2020: Control of both $PM_{2.5}$ and O_3 in
807 Beijing-Tianjin-Hebei and the surrounding areas. *Atmospheric Environment*, **224**,
808 117259, https://doi.org/10.1016/j.atmosenv.2020.117259.
809 Zhang, H. X., C. r. Chen, W. J. Yan, N. N. Wu, Y. Bo, Q. Zhang, and K. B. He, 2021:
810 Characteristics and sources of non-methane VOCs and their roles in SOA formation
811 during autumn in a central Chinese city. *Science of the Total Environment*, **782**,
812 146802, https://doi.org/10.1016/j.scitotenv.2021.146802.
813 Zhang, Y., H. Liao, X. Ding, D. Jo, and K. Li, 2018: Implications of RCP emissions on
814 future concentration and direct radiative forcing of secondary organic aerosol over
815 China. *Science of the Total Environment*, **640−641**, 1187−1204,
816 https://doi.org/10.1016/j.scitotenv.2018.05.274.
817 Zhang, Z. T., and K. C. Wang, 2020: Stilling and recovery of the surface wind speed
818 based on observation, reanalysis, and geostrophic wind theory over China from 1960
819 to 2017. *Journal of Climate*, **33**, 3989–4008.
820 https://doi.org/10.1175/jcli-d-19-0281.1.

821 Zhao, H., K. Y. Chen, Z. Liu, Y. X. Zhang, T. Shao, and H. L. Zhang, 2021: Coordinated
822 control of $PM_{2.5}$ and O_3 is urgently needed in China after implementation of the "Air
823 pollution prevention and control action plan". *Chemosphere*, **270**, 129441,
824 https://doi.org/10.1016/j.chemosphere.2020.129441.
825 Zheng, B., and Coauthors, 2015: Heterogeneous chemistry: a mechanism missing in
826 current models to explain secondary inorganic aerosol formation during the January
827 2013 haze episode in North China. *Atmospheric Chemistry and Physics*, **15**,
828 2031−2049, http://doi.org/10.5194/acp-15-2031-2015.
829 Zheng, B., and Coauthors, 2018: Trends in China's anthropogenic emissions since 2010
830 as the consequence of clean air actions. *Atmospheric Chemistry and Physics*, **18**,
831 14095−14111, https://doi.org/10.5194/acp-18-14095-2018.
832 Zhu, J., L. Chen, H. Liao, and R. J. Dang, 2019: Correlations between $PM_{2.5}$ and ozone
833 over China and associated underlying reasons. *Atmosphere*, **10**, 352,
834 http://doi.org/10.3390/atmos10070352.
835 Zong, L., and Coauthors, 2021: Large-scale synoptic drivers of co-occurring summertime
836 ozone and $PM_{2.5}$ pollution in eastern China. *Atmospheric Chemistry and Physics*, **21**,
837 9105–9124, https://doi.org/10.5194/acp-21-9105-2021.